Earth and Planetary Science Letters 519 (2019) 297–307

Contents lists available at ScienceDirect

Earth and Planetary Science Letters

www.elsevier.com/locate/epsl

Thin lithosphere beneath the central Appalachian Mountains: Constraints from seismic attenuation beneath the MAGIC array

Joseph S. Byrnes [a,*], Maximiliano Bezada [a], Maureen D. Long [b], Margaret H. Benoit [c]

[a] Department of Earth Sciences, University of Minnesota, United States of America
[b] Department of Geology and Geophysics, Yale University, United States of America
[c] National Science Foundation, United States of America

ARTICLE INFO

Article history:
Received 24 September 2018
Received in revised form 24 April 2019
Accepted 30 April 2019
Available online 31 May 2019
Editor: M. Ishii

Keywords:
Appalachian Mountains
lithosphere
attenuation
passive margin
asthenosphere
delamination

ABSTRACT

The passive margin of the eastern coast of the United States is known to be geologically active, with recently rejuvenated topography, intraplate seismicity, and volcanism of Eocene age. This study uses seismic data from the Mid-Atlantic Geophysical Integrative Collaboration (MAGIC) experiment to constrain lateral variations in the attenuation of teleseismic *P* waves beneath the central Appalachian Mountains to shed light on the structure and dynamics of the upper mantle at this "active" passive margin. We use a Monte Carlo approach to estimate variations in attenuation along with both data and model uncertainties. The quality factor of the upper mantle dramatically decreases over a distance of less than 50 km on the western side of the central Appalachian Mountains, where a low-velocity anomaly has been previously inferred. Extrinsic factors such as scattering or focusing are rejected as explanations for the observations on the basis of finite-difference waveform modeling experiments. The peak in attenuation beneath the crest of the Appalachian Mountains requires that near- to super-solidus conditions occur in the upper mantle and is co-located with volcanism of Eocene age. Our preferred interpretation is that the attenuation reflects the removal of the mantle lithosphere via delamination beneath the mountains, followed by ongoing small-scale convection.

1. Introduction

The eastern coast of North America has been a passive margin since the end of rifting between what are now the North American and African continents at approximately 210 Ma (Knight et al., 2004; Marzoli et al., 2004, 1999). After continental breakup, seafloor spreading has continued in the North Atlantic up to the present (Müller et al., 2016). This passive margin is surprisingly active. The heavily populated coastal regions are capable of hosting damaging earthquakes (Li, 2013) and volcanism has occurred episodically as late as over 100 Myr after the rift-to-drift transition (Southworth et al., 1993; Mazza et al., 2016, 2014). Stream profiles show that the Appalachian Mountains experienced a pulse of enhanced uplift between 15 and 3 Ma (Miller et al., 2013) and dynamic topography has likely changed by tens of meters in the last 3 Myrs (Rowley et al., 2013). Since the arrival of the EarthScope Transportable Array, seismic studies have revealed mantle upwelling beneath several sections of the margin (Levin et al., 2018; Lynner and Bodmer, 2017; Savage et al., 2017; Schmandt and Lin, 2014; Yang and Gao, 2018), some of which have been proposed to be caused by edge-driven convection (Menke et al., 2016).

The Mid-Atlantic Geophysical Integrative Collaboration (MAGIC) deployed an array of broad-band seismometers in a linear transect across the central Appalachian Mountains to investigate this geologically active region (Fig. 1). This EarthScope Flexible Array (FA) was deployed between October 2013 and October 2016 (see Aragon et al., 2017 for additional details). The nominal station spacing of 25 km decreased to 10 km within the Appalachian Mountains. This enables inferences about smaller scale structure in the upper mantle than would be possible using only data from the USArray Transportable Array (TA), which had a nominal station spacing of 70 km.

The MAGIC array stretches northwest-to-southeast, from the Proterozoic core of the continent to the accreted terranes on the coast (Fig. 1). The transition from Proterozoic to primarily Phanerozoic crustal units occurs where the array crosses the western edge of the mountains at the "Proterozoic Rift Margin" (PRM) (Whitmeyer and Karlstrom, 2007). The Proterozoic crust belongs to the Granite-Rhyolite province (1.5 to 1.3 Ga) with some Grenville-affinity granitoids near the mountains

---

[*] Corresponding author.
E-mail address: jsbyrnes@umn.edu (J.S. Byrnes).

https://doi.org/10.1016/j.epsl.2019.04.045

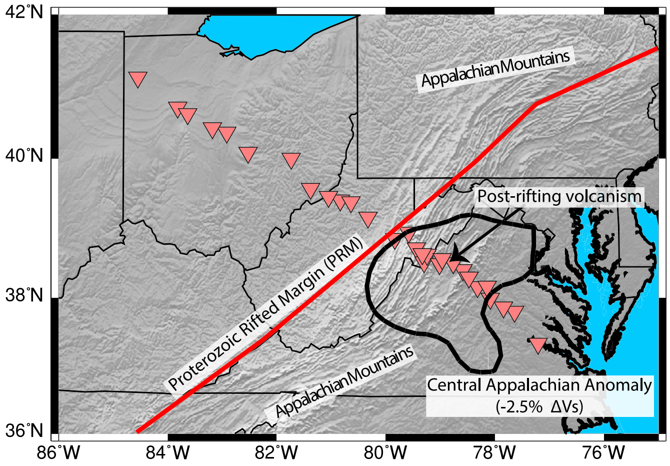

Fig. 1. Overview of the study area. Topography above sea level is shaded, regions below sea level are in blue, US state boundaries are marked as lines, and seismic stations from the Mid-Atlantic Geophysical Integrative Collaboration (MAGIC array) are marked as pink inverted triangles. The Proterozoic Rifted Margin (PRM) separates crustal ages that are predominantly Proterozoic to the west and predominately Phanerozoic to the east. The thick black line marks the -2.5% *Vs* anomaly from Schmandt and Lin (2014), which Schmandt and Lin (2014) refer to as the “Central Appalachian Anomaly” (CAA). (For interpretation of the colors in the figure(s), the reader is referred to the web version of this article.)

(Whitmeyer and Karlstrom, 2007). Rifting of the Rodinia supercontinent took place along the PRM approximately 600 Ma. The modern Appalachian Mountains were subsequently built by accretion onto Laurentia during the Taconic, Acadian, and Alleghanian orogenies, culminating in collision with Gondwana by approximately 300 Ma (Hatcher, 2010, and references therein). The deformation associated with this collision was accommodated via a Himalayan-style low-angle crustal suture (Hopper et al., 2017). The modern topography of the Appalachian Mountains is compensated by a deep but dense crustal root (Fischer, 2002; Long et al., 2019). East of the orogenic terranes there are crustal blocks acquired from Gondwana during rifting (Hatcher, 2007), though a Laurentian lower crust is possible (e.g., as in Hopper et al., 2017).

The degree to which the modern lithosphere-asthenosphere system was shaped by these episodes of rifting remains unclear; it is possible that the system has been reworked since rifting ceased. Shear-wave splitting fast polarization directions tend to follow the strike of the Appalachian Mountains (e.g., Gilligan et al., 2016; Long et al., 2016) – including at stations in the MAGIC array (Aragon et al., 2017) – as expected if lithospheric deformation during orogenesis were preserved. In contrast, there is seismic and petrologic evidence for post-rifting activity, possibly including delamination of the lithosphere (Mazza et al., 2016, 2014; Yuan et al., 2014) and ongoing asthenospheric upwelling beneath portions of the margin (Biryol et al., 2016; Levin et al., 2018; Lynner and Bodmer, 2017; Savage et al., 2017; Schmandt and Lin, 2014; Yang and Gao, 2018). One potential upwelling, the Central Appalachian Anomaly (CAA) in Schmandt and Lin (2014), is crossed by the MAGIC array (Fig. 1).

This study takes advantage of the tight station spacing of the MAGIC array to investigate small-scale variations in lithospheric mantle structure. We measure variations in the attenuation of teleseismic *P* waves from deep focus events. We infer from the results that mantle lithosphere has been removed beneath the central Appalachian Mountains, near the site of volcanism of both Jurassic and Eocene age (Evans et al., 2019; Mazza et al., 2016, 2014). Near-to super-solidus conditions are reached in the upwelling asthenosphere today, and we infer that ongoing edge-driven convection maintains upwelling to the present day.

2. Methodology for constraining seismic attenuation

We constrain upper mantle attenuation in two steps. First, we infer Δt_P^*, relative “t-star” for a *P* wave with units of seconds, by modeling changes to teleseismic *P* waves recorded by the MAGIC array (Adams and Humphreys, 2010; Bezada, 2017). We then invert for a two-dimensional model of attenuation across the study area. The quantity t^* is defined by

$$t^* = \int \frac{dt}{Q\,(t)} = \int \frac{dr}{V\,(r) * Q\,(r)} \tag{1}$$

where t is the travel-time, $Q\,(t)$ is the quality factor encountered by the phase at a given time during propagation, r is distance along the ray path, and $V\,(r)$ and $Q\,(r)$ are the velocity and quality factor along the ray path. In this study, we only measure relative changes to t_P^*, which we refer to as Δt_P^*. To show the effect of attenuation on a seismic waveform, examples of a hypothetical *P* wave that have been attenuated to greater and lesser degrees are shown in Fig. 2A. For more negative values of Δt_P^* the waveform is narrower in the time domain and contains more high frequency energy than the reference trace. As Δt_P^* increases, the high frequencies are damped and the waveform broadens.

We measure Δt_P^* by modeling the waveforms of the first arriving *P* waves for 6 events recorded by the MAGIC array. We restrict our analysis to events with hypocentral depths greater than 200 km, and to station-event pairs separated by distances between 30 and 90°. The 6 events are described in Table 1. A total of 141 measurements of Δt_P^* were made with waveforms filtered between 0.02 and 3 Hz; *P* waves observed at this distance are typically dominated by energy near 1 Hz. We first make an estimate of the unattenuated source-time function, and match attenuated versions of this estimate to recordings of the first arriving *P* waves with a grid search over Δt_P^* (Bezada, 2017). Example seismograms compared to attenuated synthetics are shown in Fig. 2B.

To analyze the results, we invert for a two-dimensional surface that is consistent with the measured values of Δt_P^*. In this study the surface is nearly one-dimensional and along strike of the array. Since few events are usable, we cannot constrain a three-dimensional model. However, attenuation primarily occurs at asthenospheric depths, where the ray-paths of the *P* waves become nearly vertical. We therefore map variations in Δt_P^* in two dimensions before exploring hypothetical depth variations in Q_P in a later section. We do not consider crustal structure; a 1 km thick sedimentary package will only contribute a Δt_P^* of 0.015 s, and Qp rapidly increases with greater thickness (Campbell, 2009).

We modify the method of Bezada (2017) for inverting for a two-dimensional surface for Δt_P^* from a least-squares solution to a Bayesian Monte Carlo inversion. We use this approach for three reasons. First, this approach provides an estimate of the uncertainty of the data by including the uncertainty as a free parameter in the Monte Carlo search. Previous studies have shown that the search will converge to the correct uncertainty if the search seeks to maximize the likelihood function (Bodin et al., 2012a, 2012b; Eilon et al., 2018; Malinverno and Briggs, 2004). Because the uncertainties are estimated by the inversion, a second advantage of this approach is that *a priori* weights on the smoothness or magnitude of the final solution are not needed. Heuristically, the inversion searches for a model that is as sharp but no sharper than is needed to explain the data. Third, because a wide range of models are evaluated during the search, the uncertainty of the model can be estimated from the width of the distribution of Δt_P^* values in all acceptable models.

The inversion that we implement has been described in detail elsewhere (Bodin et al., 2012a, 2012b; Eilon et al., 2018; Olugboji et al., 2017) and our approach does not significantly diverge from these studies. The inversion begins by creating a model

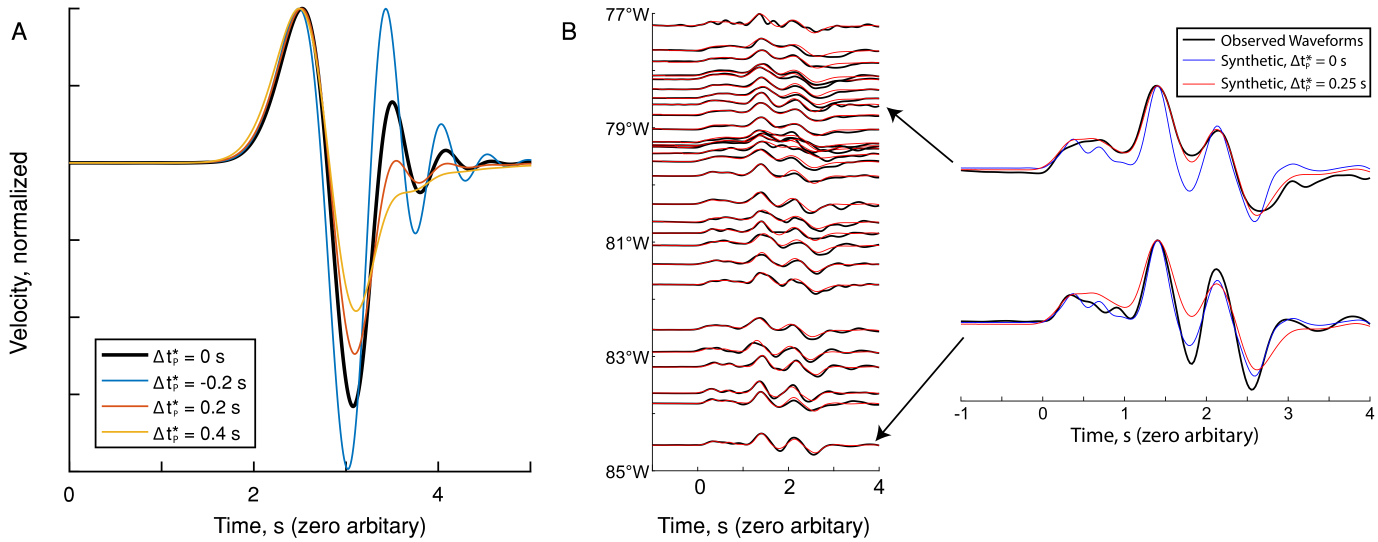

Fig. 2. Demonstration of the time-domain method for Δt^*_P. Examples of attenuated synthetic and real waveforms. A) Example of a hypothetical *P* wave that has undergone different degrees of attenuation. B) Comparison between observed seismograms and their best fitting attenuated synthetics. The observed seismograms are in black, and are for a magnitude 5.8 event in the vicinity of Hokkaidō (Line 2 of Table 1). The best fitting synthetics are in red. Two seismograms are highlighted on the right, and are compared with an unattenuated and attenuated synthetic.

Table 1
Details of the events used in this study.

Region	Latitude (degrees)	Longitude (degrees)	Origin time (UTC)	Magnitude	Depth (km)	σ (s)
Argentina	−22.2087	−66.0261	2016-08-04 14:15:13.090	6.2	270	0.11
Hokkaidō	47.6981	146.9212	2016-07-23 01:00:20.940	5.8	408	0.13
Bolivia	−19.7597	−63.3288	2016-01-14 03:25:28.270	6.1	583	0.11
Hokkaidō	44.4761	141.0867	2016-01-11 17:08:03.920	6.2	238	0.18
Brazil	−9.1825	−71.2574	2015-11-26 05:45:18.400	6.7	603	0.17
Argentina	−23.1125	−66.688	2015-02-11 18:57:22.460	6.7	223	0.11

with a random number of nodes with randomly assigned values of Δt^*_P. The fit of this model to the data is evaluated after nearest-neighbor interpolation; that is, we use Voronoi diagrams as the basis function for constructing the models. A new model is then created by taking one of 5 possible steps: a "birth" step where a new node is introduced, a "death" step where a node is removed, a "move" step where a node is moved to a new location, a "change" step where the Δt^*_P of a node is changed, or a "hyperparameter" step where the uncertainty of the data is changed within the context of some parameterization. An example of a parameterization for the data uncertainty would be to use one uncertainty for all of the input data, which would introduce one free parameter, or to use one uncertainty per event, which in this study would introduce 6 free parameters. The acceptance criteria for new models (Bodin et al., 2012a, 2012b) biases the search towards accepting simpler models if the misfit is not worsened, and towards a level of uncertainty where a more complex model cannot significantly improve the fit to the data. For all inversions shown here, we iterate 100 parallel instances of the search over 1e5 models and keep the set of models with the 5% highest likelihoods.

We then make a probability distribution function (PDF) every 5 km along the array by normalizing a histogram of the Δt^*_P in the ensemble of models at each point along the array with a bin spacing of 0.001 s. The width of the PDFs provides an estimate of the uncertainty of the model. Shen and Ritzwoller (2016) showed that the standard deviation of the ensemble can be as much as a factor of 4 larger than the standard error. This is because the ensemble of models defines a PDF with a mean, median, and mode that are well-defined regardless of the width of the distribution. We confirm this factor of 4 for our results, and show uncertainties by dividing the standard deviation of the PDFs by two, which gives twice the standard error (i.e., the 95% confidence interval) below. We stress that this uncertainty is the "model" uncertainty and distinct from the "data" uncertainty, which is the noise in the input Δt^*_P values.

To demonstrate the validity of the inverse approach, we show two sets of synthetic inversions in Fig. 3. The synthetic tests use the same set of station-event pairs as used with the MAGIC array. The first set, in Fig. 3A and 3B, show a pair of inversions for one-dimensional synthetic datasets. The values of Δt^*_P are drawn from the true model and Gaussian noise was added with a standard deviation of 0.025 s. The contours show the PDFs from the inversion. For this pair of inversions, the data uncertainty was fixed during the search to the true value. In the first test, shown in Fig. 3A, Δt^*_P in the input model increases linearly from −0.2 s on the western edge of the array to 0.2 s on the eastern edge. In the second test, shown in Fig. 3B, Δt^*_P is zero except in two sharply defined boxes with Δt^*_P of −0.2 and 0.2 s. The inversion process is identical in each case, despite the dramatic difference in the gradients of the model. Were the model smoothness fixed *a priori*, this pair of models would demand different configurations of the inversion. Instead, our approach successfully recovered both a linear trend and steps in Δt^*_P with an identical configuration. The only issue is that the linear model is recovered as steps between −200 and 0 km where gaps in station coverage reach nearly 50 km; this occurs because nearest neighbor interpolation was used to evaluate the models.

In Fig. 3C, we reinvert the "step" model while inverting for the uncertainty of the data. Noise was added with standard deviations of 0.075 s for the first set of three events, and with a standard de-

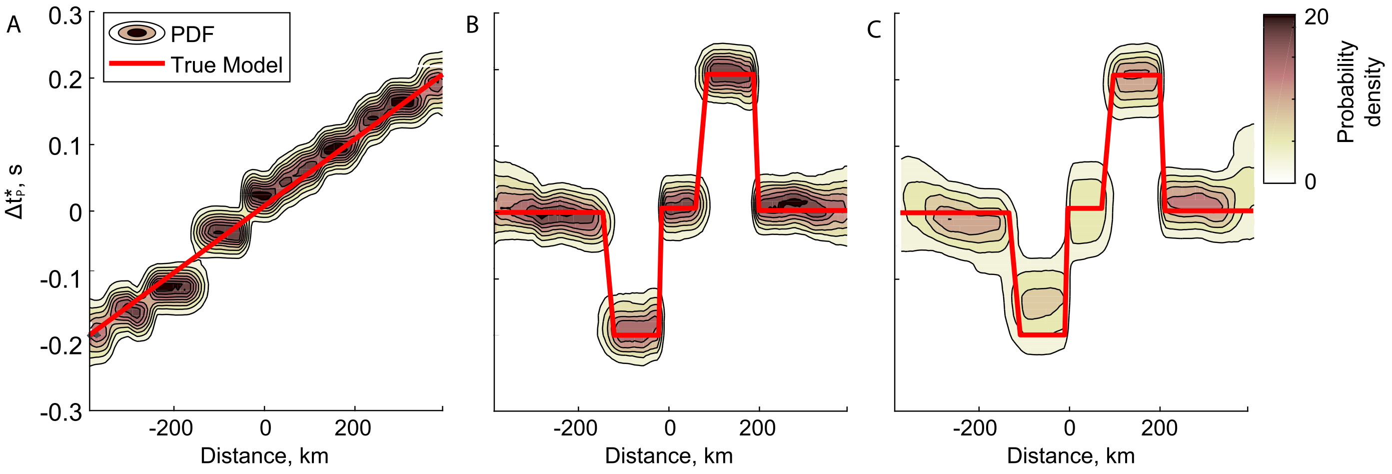

Fig. 3. Synthetic tests of the inversion in 1D. Probability distribution functions from the inversion are contoured, and the red line shows the input ("true") model. See text for description of the separate inversions.

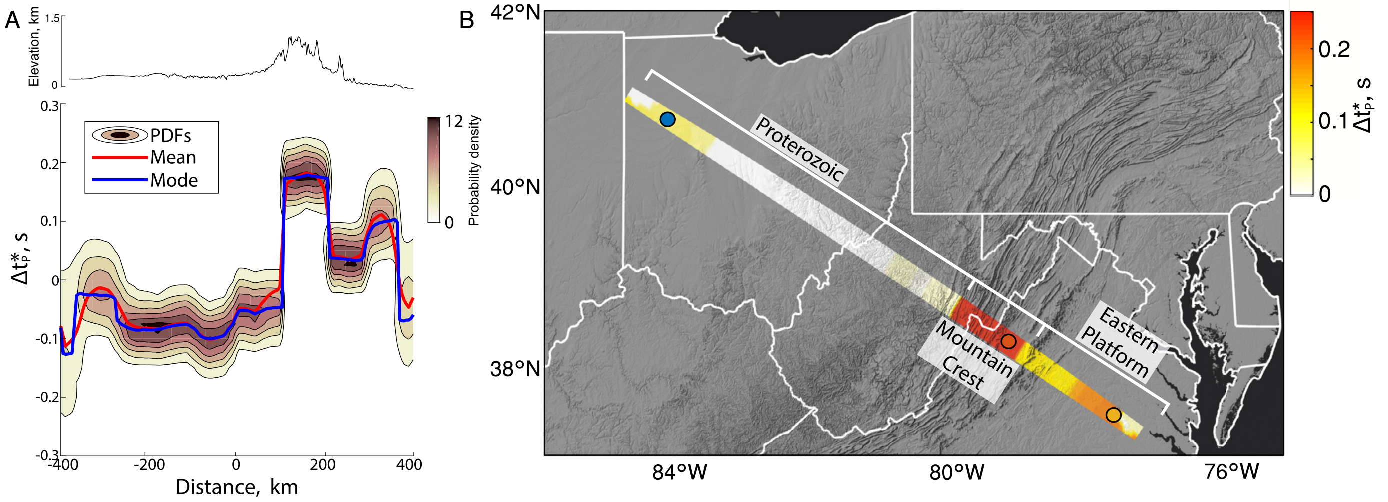

Fig. 4. Preferred model for Δt_P^*. A) The probability distribution function from the preferred inversion is contoured, with the mean and mode marked in red and blue, respectively, and topography along the array shown on top. B) The mode of the preferred model in map view. Topography is shaded and Δt_P^* is the mode of the PDF from the inversion (panel A). The Proterozoic, Mountain Crest, and Eastern Platform domains are defined by text and the white lines. For plotting purposes, the values at or below the average of the Proterozoic domain are set to zero. Circles show the locations of shear-wave velocity profiles in Fig. 7.

viation of 0.15 s for the second set of three events. This level of noise is high, as the size of the two steps is only 0.2 s, and so requires an inversion that properly handles uncertainties. We invert for the model and one uncertainty per event. The true model is well recovered with wide PDFs. For the first three set of events, the recovered uncertainties are 0.10 s, 0.08 s, and 0.08 s; twice the standard error for these values is 0.02 s. For the second set of three events, the recovered uncertainties are 0.2 s, 0.16 s, and 0.16 s; twice the standard error for these values is 0.03 s. Hence, the quality of the data can be estimated well. We conclude that we have a sufficiently large dataset that the true model can be recovered along with one uncertainty for each event.

3. Results and comparison with previous studies

We present our preferred model for variations in seismic attenuation across the MAGIC array in Fig. 4. We present PDFs along the center of the model in 1D in Fig. 4A, and the mode of the PDFs in map view in Fig. 4B. The model in Fig. 4 can be categorized into three domains with distinct signatures in attenuation – the "Proterozoic", the "Mountain Crest", and the "Eastern Platform" domains (Fig. 4).

In the preferred inversion, Δt_P^* is 0.26 s and 0.13 s in the Mountain Crest and Eastern Platform domains, respectively, relative to mean of the Proterozoic domain. The Mountain Crest domain is coincident with the CAA in the velocity model of Schmandt and Lin (2014) (Fig. 1); however, we are not aware of a prior detection of the local maximum in seismic attention at the CAA (cf., Bao et al., 2016; Cafferky and Schmandt, 2015; Hwang et al., 2009). The uncertainty on the model allows the transition between the Proterozoic and Mountain Crest domains to be up to 50 km wide (Fig. 4A). The width of the gradient on the eastern side of the Mountain Crest domain is negligible. Smaller variations in Δt_P^* are present within each domain, but are poorly constrained. The average uncertainty of the model, twice the standard error, is estimated at ±0.015 s. This implies an uncertainty on the differences between the domains of ±0.02 s. Four alternative models are shown in the Supplemental Section 1: with a uniform data uncertainty, with a station-specific data uncertainty, with linear interpolation, and with "spectral slope" measurements (Teng, 1968). These four models give different fluctuations within the three domains, but differences between the domains are slightly greater than or within error of the preferred model.

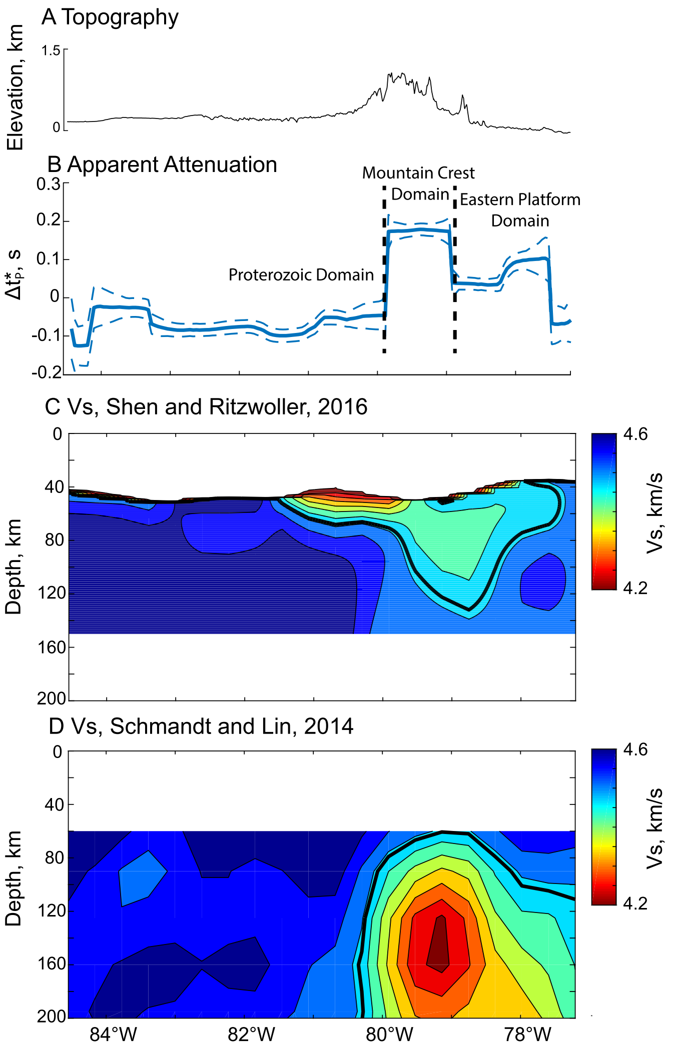

Fig. 5. A comparison of datasets along the strike of the MAGIC array. A) Topography. B) Variations in Δt_P^* (cf. Fig. 2) with the inner 66% of the probability distribution marked by the dashed lines; this approximates the 95% confidence interval for the model (see text for discussion). The values of Δt_P^* have been demeaned, as opposed to pegged to zero, to allow for the plotting of the uncertainty. B) Shear-wave velocity beneath the MAGIC array in the model of Shen and Ritzwoller (2016). This study used data from both receiver functions and Rayleigh wave phase velocities. Shear-wave velocities above the Moho are not shown and the model is not defined below 150 km depth. D) Shear-wave velocity beneath the MAGIC array in the model of Schmandt and Lin (2014). The model is not defined above 60 km depth. The study of Schmandt and Lin (2014) solved for relative variations in velocity, and we use their reference velocity model of AK135 to convert the anomalies to absolute values of *Vs*.

The uncertainties of the data are given as standard deviations in the last column of Table 1. Typical values are between 0.11 and 0.13 s, although two events have higher uncertainties and were thus down-weighted during the inversion. These uncertainties are high relative to the range of the final model, and can be plausibly explained by signal-generated noise (Bezada et al., 2019).

Comparing our results to lateral variations in topography (Fig. 5A, B) and shear wave velocity from both surface waves and body waves (Fig. 5C, D), it is clear that all three parameters exhibit first-order variations among the three distinct domains. For the comparisons, we use the joint surface wave-receiver function model of Shen and Ritzwoller (2016) (5C, hereafter SR16) and the body-wave model of Schmandt and Lin (2014) (5D, hereafter SL14). In the Proterozoic domain, where the least attenuation was observed, topography is relatively flat and *Vs* is consistently above 4.5 km/s in both velocity models. Beneath the Mountain Crest domain, the two velocity models are similar above 90 km depth but diverge below. In SR16, variations in subcrustal velocity peak near 90 km depth, neglecting a localized anomaly at the base of the Moho centered on 80.5°W (Fig. 5C). In contrast with the SR16 model, in SL14 the low-velocity anomaly reaches a minimum of 4.25 km/s at a depth of 150 km. We attribute the difference to the data used to construct each model. The phase velocities of Rayleigh waves, used by Shen and Ritzwoller (2016), have a markedly reduced sensitivity to *Vs* anomalies at a depth of 150 km, while the travel times of body-waves used by Schmandt and Lin (2014) remain reliable at these depths (e.g., Villagómez et al., 2007, 2014). Taken together, the seismic tomography models reveal a low-velocity anomaly beneath the Mountain Crest domain beneath a high velocity lid.

Beneath the Eastern Platform domain, topography is relatively smooth and lies at a lower elevation than within the Proterozoic domain. Δt_P^* has intermediate values and both velocity models feature *Vs* intermediate between the Proterozoic and Mountain Crest domains. Neither velocity model displays strong anomalies below 100 km depth beneath the eastern platform.

To summarize, our attenuation model exhibits strong lateral variations across the array, with three clear domains of distinct Δt_P^*. There are clear correlations among topography, Δt_P^*, and *Vs* along the MAGIC array. We attribute a slight westward offset of the Δt_P^* maximum relative to the *Vs* minima to the refined station spacing of the MAGIC array. West of the PRM (Fig. 1), *Vs* is high and Δt_P^* is low. Where the array crosses the Appalachian Mountains into Phanerozoic crust, a local maximum in Δt_P^* correlates with the location of the CAA (Fig. 1). Continuing eastward, both seismic velocity and attenuation in the Eastern Platform domain are intermediate between the other two regions.

4. Discussion

4.1. Physical state of the lithosphere-asthenosphere system

In this section we combine previous tomographic results and our new results for attenuation to constrain the physical state of the upper mantle beneath the MAGIC array. The Δt_P^* results motivated a partition of the MAGIC study area into three domains (Fig. 4). Fig. 6 shows *Vs* profiles from SR16 and SL14 within each domain and from the tectonic domains of Lekić and Romanowicz (2011a). Lekić and Romanowicz (2011a) constructed *Vs* profiles for "Old continental", "Modified Continental", and "Young Oceans" domains via a cluster analysis of *Vs* from global tomographic models (Lekić and Romanowicz, 2011a, 2011b). These names are used for clarity and are not from the original study. The "Old Continental" (CR2 in Lekić and Romanowicz, 2011a) cluster generally corresponds to continental interiors surrounding a slightly faster cluster (CR1) at continental centers. The "Modified Continental" cluster (CR3) generally represents continental regions that have undergone deformation in the Phanerozoic, such as Indonesia or Northern China. The "Young Oceans" (OR1 in Lekić and Romanowicz, 2011a) cluster includes the mid-ocean ridge system and magmatically active regions like the Western United States.

We use the comparison in Fig. 6 to place the three subdivisions of our study area in a global context. The Proterozoic domain (Fig. 4) has *Vs* typical of the "Old Continental" cluster. At 75 km depth, the Mountain Crest has similar *Vs* to the "Modified Continental" cluster, and the Eastern Platform is intermediate between the "Old Continental" and "Modified Continental" clusters. At greater depths, the two velocity models diverge beneath the Mountain Crest and Eastern Platform domain due to the presence of the CAA. Velocity beneath the Mountain Crest domain (the CAA) reaches the minimum *Vs* in the "Young Oceans" cluster. Beneath the Eastern Platform, *Vs* merges with the "Modified Continental"

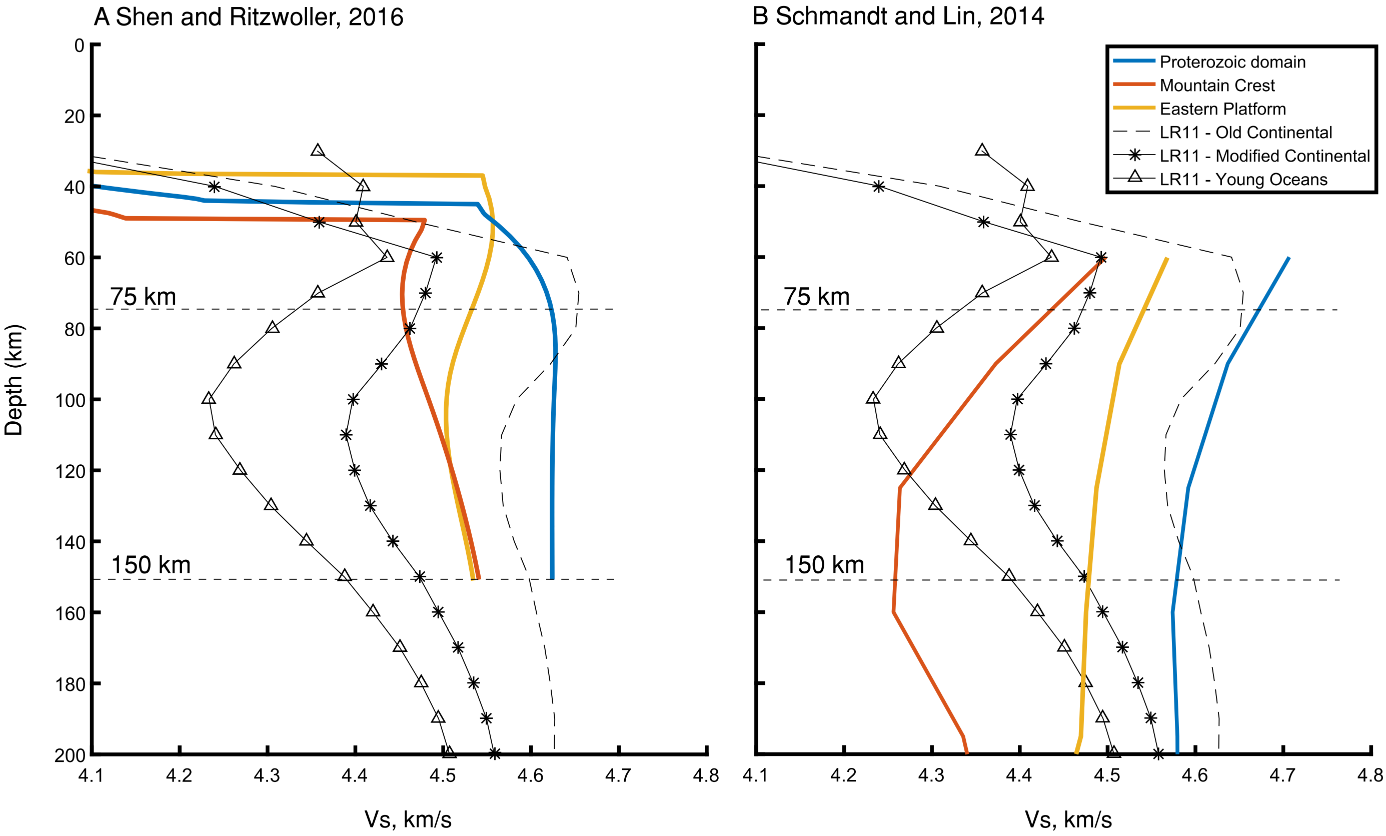

Fig. 6. Shear-wave velocity profiles from each of the domains compared with the clusters of Lekic and Romanowicz (2011a, 2011b). See Lekić and Romanowicz (2011a) and text for discussion and definition of the clusters. A, B) Comparison of the clusters of Lekić and Romanowicz (2011a) with shear-wave velocity profiles at the three circles with matching colors in Fig. 2 from the models of Shen and Ritzwoller (2016) and Schmandt and Lin (2014), respectively.

cluster at a depth of 150 km and is marginally faster than the cluster at shallower depths.

Before interpreting the values Δt_P^* in terms of the quality factor of the upper mantle, we must consider if "extrinsic factors" can explain the apparent attenuation. We explore and reject two possible sources of Δt_P^* artifacts in Supplemental Section S2. The first is scattering of the wavefield (Richards and Menke, 1983; Wu, 1982). We show with finite difference experiments that Δt_P^* artifacts produced by scattering can be detected by comparing results from our time domain method with results from the frequency domain method of Teng (1968), since the time domain method is relatively insensitive to the effects of scattering (Bezada, 2017). The second effect is focusing by variations in seismic velocity (Allen et al., 1999; Dalton and Ekström, 2006), which we show produces Δt_P^* artifacts on length scales shorter than the width of our three domains. We interpret the results only in terms of Qp for the remainder of the paper.

We next use Δt_P^* from the Mountain Crest and Eastern Platform domains to infer possible values of Qp in the upper mantle. The *P* wave data used in this study only constrain the path-integrated attenuation, and so we explore hypothetical variations in Qp with depth (Fig. 7) in lieu of a three dimensional tomography model for Qp. We define two layers in the upper mantle from 40 to 90 km and 90 to 200 km based on depths of the high velocity lid and the CAA. We assume PREM values of Qp for the lithosphere within the Proterozoic domain, and use a 200 km thick lithosphere in this region (Abt et al., 2010; Biryol et al., 2016; Schaeffer and Lebedev, 2014; Yuan et al., 2014) as the reference for our Δt_P^* measurements. We then compute the predicted attenuation for each model with equation (1), and color as bands the regions that explain the Δt_P^* results for the Mountain Crest and Eastern Platform regions within the error of the difference between the domains (±0.02 s).

If Qp were constant between 40 and 200 km depth (black line in Fig. 7), we estimate a Qp between 66 and 84 for the Mountain Crest and 130 to 160 for the Eastern Platform. However, since *Vs* is decreasing with increasing depth (Fig. 5), we consider a decrease in Qp with increasing depth more likely than a constant Qp model. This motivates a second set of estimates, which are to the right of the black line in Fig. 7. The end-member case features Qp in the deeper layer between 50 to 63 beneath the Mountain Crest and 103 to 125 beneath the Eastern Platform.

We next explore possible variations in lithospheric thickness beneath the Proterozoic domain. The calculation for Fig. 7A assumed a PREM-like lithosphere of 200 km thickness west of the PRM. Deviations from these assumptions have a weak effect if the average Qp remains high, and so a wide range of deviations are possible. For example, halving the average Qp from 2000 to 1000 over 200 km causes a Δt_P^* of only 0.02 s (Fig. 7B). Fig. 7B shows the maximum thinning of the lithosphere from a reference thickness of 200 km allowed by an uncertainty on Δt_P^* of ±0.02 s. This calculation is reductive, because the lithosphere-asthenosphere boundary in this region may be diffuse (Abt et al., 2010), but 45 km of variability in lithospheric thickness can be accommodated under these assumptions if Qp values from PREM are assumed.

We now discuss how constraints on *Vs* and Qp could relate to the physical properties of the upper mantle. In Fig. 8, we explore if *Vs* and Qp can be explained in terms of temperature and grain size using the Very Broadband Rheology Calculator (Holtzman, 2016), which applied the model of Jackson and Faul (2010) to an imposed thermal structure for the region. First, for Fig. 8A, we assume a 100 km thick, conductively cooled plate (Abt et al., 2010) for the

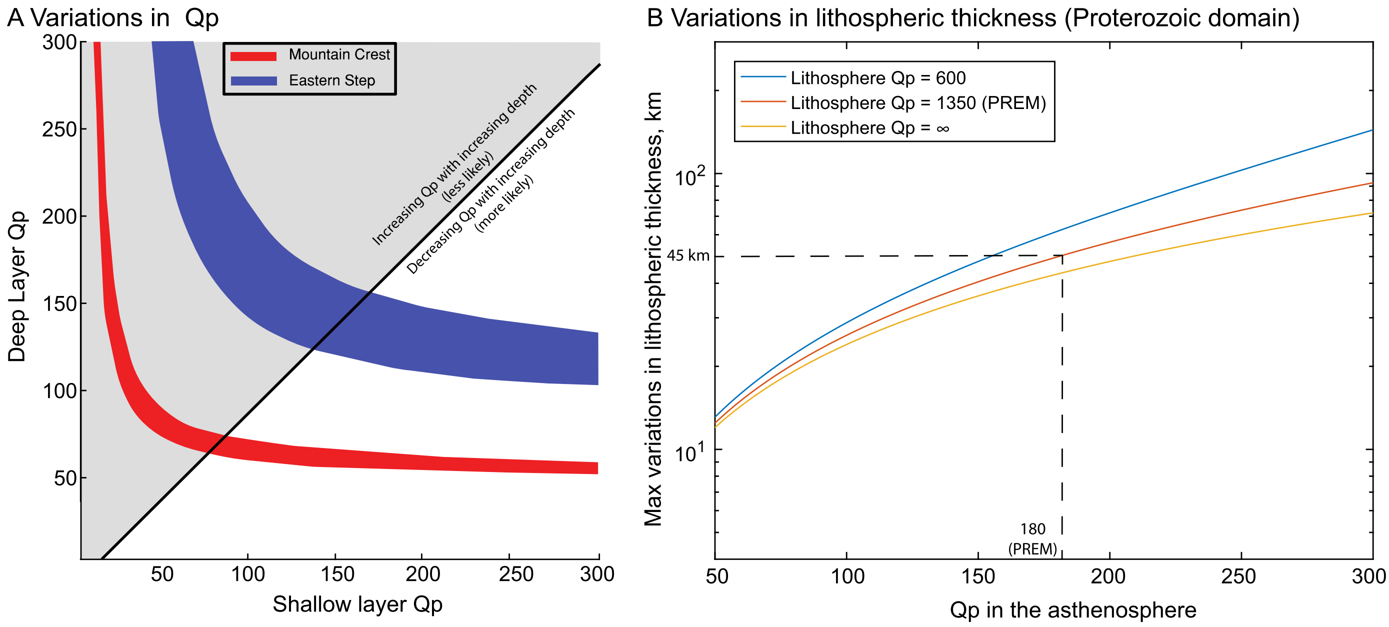

Fig. 7. Seismic interpretations of the Δt_P^* results. A) Range of Qp relative in a shallow (40 to 90 km) and a deep (90 to 200 km) layer beneath the Mountain Crest and Eastern Platform domains. The black line marks the model parameters for which Qp does not vary with depth, and models to the left of this line are considered less likely (see text for discussion). B) Maximum allowed variations in lithospheric thickness, given the error estimates on the preferred Δt_P^* model in Fig. 3B. "Lithosphere" in this figure refers to a high Qp lid.

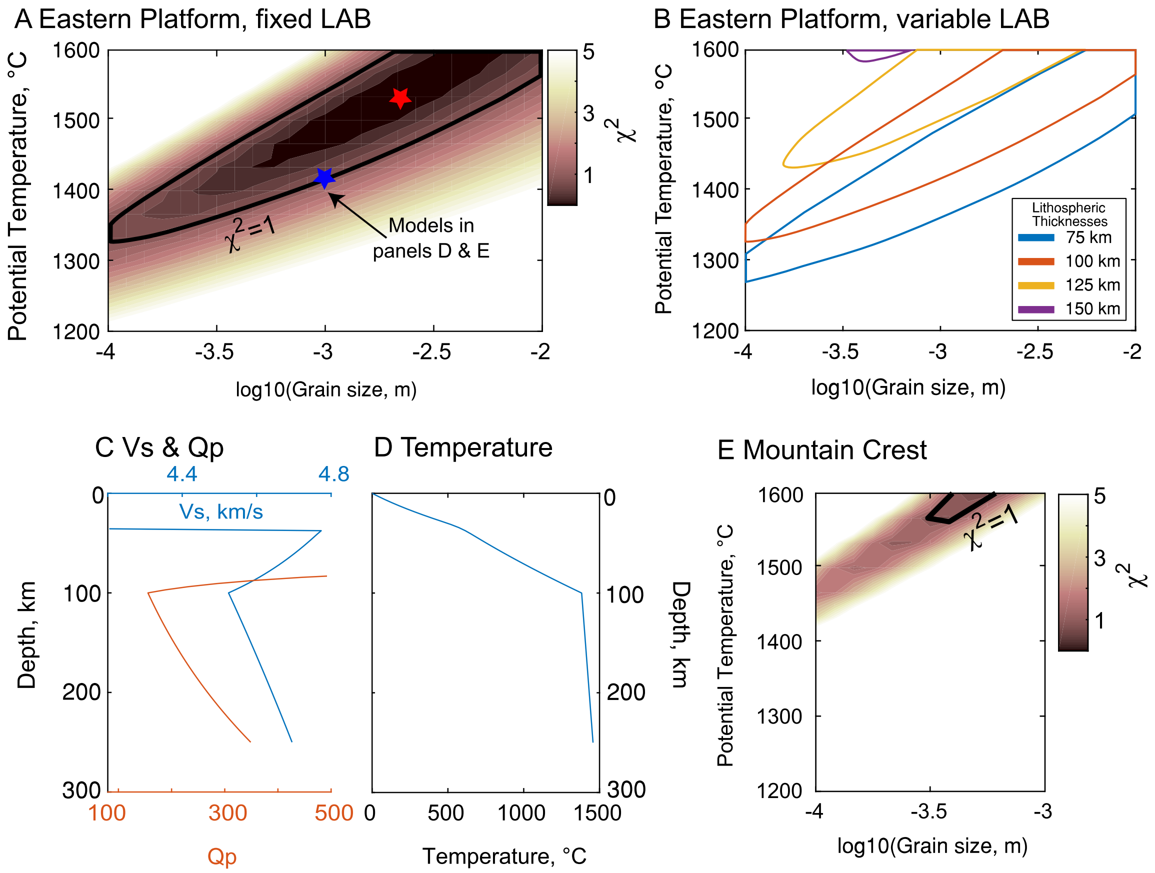

Fig. 8. Physical interpretation of the seismic results for the Eastern Platform and Mountain Crest domains. A) Fit of the model of Jackson and Faul (2010) to the *Vs* and attenuation results, respectively, assuming different potential temperatures and grain sizes for the upper mantle beneath the Eastern Platform. Red star marks the best fitting model, and blue star marks an acceptable and more physical reasonable model. B) Contours of the $\chi^2 = 1$ region when assuming a range of lithospheric thicknesses for the Eastern Platform region. A thickness of 100 km was assumed for panel A. C) *Vs* and Qp profiles for the model marked by the blue star in Panel A. D) Temperature profile associated with the model marked by the blue star in Panel A. E) Repeat of the search in panel A for the Mountain Crest region.

Eastern Platform, above an adiabatic asthenosphere. The predicted Vs and Qp values for models with varying potential temperatures and grain sizes were evaluated by fitting the mean predicted Vs between 60 and 200 km depth from SL14, and fitting the predicted t_P^* value for a vertically propagating P wave from 200 km depth to the base of crust at 37 km depth (Shen and Ritzwoller, 2016).

Fig. 8A shows the fit of the predicted values to the observed values as χ^2, defined here as

$$\chi^2 = 0.5 * \left[\frac{(Vs_{predicted} - Vs_{observed})^2}{\sigma_{Vs}} + \frac{(t^*_{p\,predicted} - t^*_{p\,observed})^2}{\sigma_{t^*}} \right] \tag{2}$$

where σ_{Vs} and σ_{t^*} are estimates of the uncertainty for Vs and t_p^*. We do not have a strict estimate of the uncertainty on Vs for SL14. We estimate an uncertainty of 0.05 km/s, which is equivalent to assuming a misfit to S wave travel times of 0.25 s for a 140 km long column of the upper mantle.

The predicted seismic profiles are sensitive to both variations in potential temperature and variations in grain size. This is indicated by the nearly 45° slope of the $\chi^2 = 1$ contour. The $\chi^2 = 1$ contour for models with different lithospheric thickness are shown in Fig. 8B. With thicker lithosphere, the potential temperature and grain size must be reduced in the consequently thinner asthenosphere. For a thickness greater or equal than 150 km, only unrealistic values for the asthenosphere can explain the data. The best fitting model with a lithospheric thickness of 100 km (red star in Fig. 8A) features a potential temperature above 1500 °C and a grain size of slightly below 1 cm. This grain size is reasonable (Abers et al., 2014 and references therein), but a potential temperature above 1500 °C is unreasonable for this region, unless the temperature is markedly higher than the Eocene potential temperature of 1412 ± 25 °C (Mazza et al., 2014), and the ambient asthenosphere (Sarafian et al., 2017). However, the fit for a model with a potential temperature of 1400 °C and a grain size of 1 mm (the blue star in Fig. 8A) is acceptable (i.e. its χ^2 is near 1). The predicted Vs and Qp profiles are shown in Fig. 8C, assuming a Qp/Qs ratio of 2.25 (Karato and Spetzler, 1990), and the thermal structure is shown in Fig. 8D. Attenuation primarily occurs below the 100 km thick plate (Abt et al., 2010), since anelastic effects are not important when temperature is below approximately 1000 °C (Jackson and Faul, 2010). The maximum and minimum values of the predicted Vs are not reached in the Vs profile of SL14. However, because tomographic inversions are subject to smoothing and damping constraints, the minimum and maximum values will likely be obscured; this inference is supported by higher Pn velocities (Buehler and Shearer, 2017) in this region than in the model of Schmandt and Lin (2014).

We consider the prediction of the model of Jackson and Faul (2010) for a small grain size, potential temperature similar to the ambient mantle, and 100 km thick plate an adequate explanation for the observed seismic structure of the upper mantle beneath the Eastern Platform. We cannot exclude the hypothesis that the mantle is cooler, with water or melt (as in Rychert et al., 2005) below the LAB reducing Vs and Qp, but neither are such additional factors required. A likely thickness for the lithosphere in this region is between 100 and 125 km, a value that is consistent with some (Evans et al., 2019) though not all magnetotelluric results for the region (e.g., see Gribenko and Zhdanov, 2017; Murphy and Egbert, 2017).

Unlike in the Eastern Platform, constraints from the Mountain Crest domain require that melting processes be invoked. The inferred values of Qp in this region are lower than the model of Jackson and Faul (2010) can explain unless unrealistic temperature and grain sizes are assumed (see Abers et al., 2014 for a discussion). For Fig. 8E, we repeat the process used for Fig. 8A with a 60 km thick plate and 50 km thick crust for the Mountain Crest Region. Choosing this thin lithospheric thickness will result in higher mean Qp in the asthenosphere. The required potential temperatures are higher than in the hottest plumes (Herzberg et al., 2007). A thin lithosphere was assumed in the calculation to maximize estimates of Qp, but even so Qp is too low. Melting processes could explain the observations in several ways. The first we discuss is a hypothetical "premelting" effect. The model of Yamauchi and Takei (2016) predicts that attenuation increases at slightly subsolidus temperatures, and does not include any further enhancement at or above the solidus. This model predicts a Vs and Qp of 4.2 km/s and 102 under the following assumptions: the upper mantle at 150 km has a potential temperature of 1400 °C, the upper mantle is at the solidus, the incoming wave has a period of 0.5 s, the upper mantle viscosity is 10^{18} Pa s, and the Qp/Qs ratio is 2.25. Period and viscosity trade off due to Maxwell-frequency scaling (see Yamauchi and Takei, 2016; Takei, 2017 for a discussion) and because of this trade-off we do not further consider variations in either parameter.

A Qp of 102 is higher than the allowed values beneath the Mountain Crest region (50 to 84), and so we consider three additional possibilities. The first is that another physical process, possibly the presence of melt in an attenuating configuration (Abers et al., 2014; Hammond and Humphreys, 2000), is required to reduce Qp beyond the "premelting" effect (Yamauchi and Takei, 2016). Second, Qp/Qs may be lower than 2.25 because of some contribution from bulk attenuation. A Qs of 45 is the direct quantity predicted by the model of Yamauchi and Takei (2016), which implies a Qp of 45, 67, 79, and 90, for Qp/Qs ratios of 1, 1.5, 1.75 and 2. This covers our estimated range beneath the Mountain Crest region, and melt could theoretically enhance bulk attenuation (Hammond and Humphreys, 2000). Third, the amplitude of the low-Vs anomaly may be greater than in the model of Schmandt and Lin (2014). If Vs were 4.15 or 4.1 km/s at 150 km depth, then the model of Yamauchi and Takei (2016) predicts a Qp (for Qp/Qs of 2.25) of 81 and 68, which are consistent with the values allowed beneath the mountain crest region.

We conclude that the asthenosphere is under solidus to supersolidus conditions beneath the Mountain Crest. Our results do not require the present of *in-situ* melt, as the "premelting" effect of Yamauchi and Takei (2016) can explain the anomaly with some qualifications, but we cannot strictly reject the presence of melt. We also note that the conductivity of the upper mantle is sufficient to require *in-situ* melt (Evans et al., 2019). However, we can say that unlike beneath the Proterozoic or Eastern Platform domains, the hypothesis that the upper mantle beneath the mountains is under sub-solidus conditions can be rejected.

4.2. Geodynamic processes

We propose a geodynamic scenario that is consistent with the seismic and petrologic (Mazza et al., 2014, 2016) results for the region. To summarize, we infer the loss of the continental lithosphere beneath the Central Appalachians and that the resulting lithospheric cavity has been sustained by small-scale convection. We discuss in detail two major features of this scenario (topography on the lithosphere-asthenosphere boundary and the inferred upwelling of the asthenosphere beneath the crest of the mountain range), and how the seismic constraints inform our interpretation.

In our cartoon summarizing the major features of our conceptual model (Fig. 9), the lithosphere west and east of the Appalachian Mountains is referred to as the "Proterozoic" (dark blue) and "Phanerozoic" (sky blue) lithosphere, respectively. This interpretation is based on the predominant ages of the overlying crust (Fig. 1, Whitmeyer and Karlstrom, 2007). For this study, the term

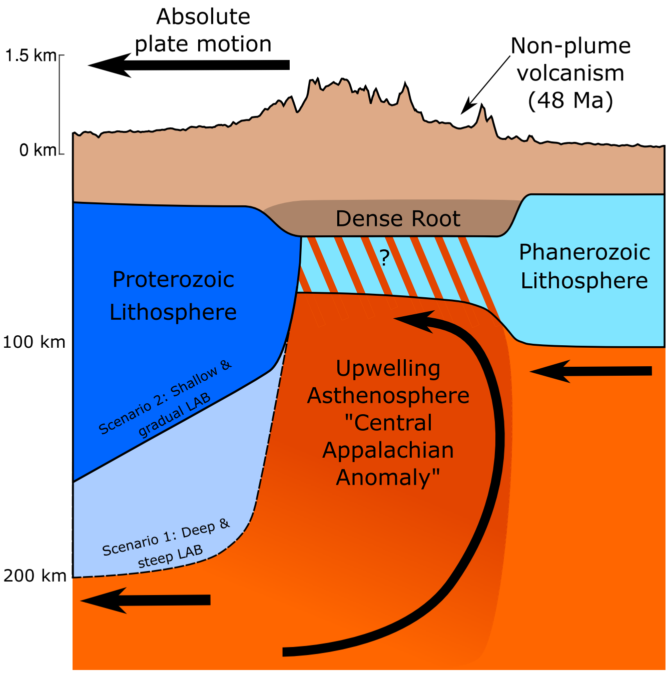

Fig. 9. Geodynamic scenario for the MAGIC study area. Bold and straight arrows show the motion of the North American plate in a hotspot reference frame, and the thin arrow shows the location of Eocene volcanism. The crust is in brown with topography on top and estimated crustal thickness on bottom, Proterozoic and Phanerozoic lithosphere are in dark and sky blue, the Central Appalachian Anomaly (CAA) and ambient asthenosphere are in dark and light orange, respectively. Flow lines are illustrated by the curved arrow in the asthenosphere. Two possible scenarios for the thickness of Proterozoic lithosphere are illustrated with shades of blue and text. The striped Phanerozoic lithosphere shows where the relative extents of Phanerozoic lithosphere and the CAA is ambiguous.

“Proterozoic” lithosphere could be interchanged with the “Old Continental” cluster of Lekić and Romanowicz (2011a) and “Phanerozoic” lithosphere could be interchanged with the “Modified Continental” cluster (as discussed in Section 4.1), though this terminology should not be generalized to the clusters on a global scale or to the North American continent as a whole.

Moving from west to east, the variations in attenuation along the MAGIC array require abrupt changes in the thickness of the lithosphere. The North American lithosphere is known to reach depths greater than 200 km (Abt et al., 2010; Biryol et al., 2016; Schaeffer and Lebedev, 2014; Yuan et al., 2014), but seismic studies often infer thinner lithosphere near the coasts (Rychert et al., 2005, 2007; Abt et al., 2010). The tight station spacing along the MAGIC array provides an opportunity to study where and how rapidly the lithosphere thins, as reflected in upper mantle attenuation. Two possible scenarios for the lithospheric architecture beneath the MAGIC array are illustrated in Fig. 9, based on the calculations discussed in Section 4.1. In scenario 1, the lithosphere rapidly thins (going from west to east) beneath the western edge of the Appalachian Mountains. This scenario is identified in Fig. 9 as the “Deep and Steep LAB”. The model uncertainties allow a maximum width of the transition of 50 km. In this scenario, continental breakup and any subsequent small-scale convection left preexisting lithosphere in-board of the rift largely unmodified. The second scenario invokes gradual thinning of the Proterozoic lithosphere from west to east (Fig. 7B). The most likely pattern for thinning is gradual west-to-east thinning of the Proterozoic lithosphere (Evans et al., 2019), although our results allow for thinning to occur anywhere beneath the Proterozoic domain. In this scenario, the thinning may have occurred during Proterozoic rifting, or may have occurred after rifting due to convection associated with the CAA.

The lithosphere thickens near the eastern edge of the Appalachians. The results only allow a narrow width of the transition of approximately 25 km. We inferred above that a lithospheric thickness near 100 km and a dry, melt free upper mantle (Jackson and Faul, 2010) are sufficient to explain both the Vs and Qp in this region. However, for our preferred Vs and Qp model (Fig. 8D) to be valid, the maximum and minimum values of Vs at the base of the crust and lithosphere, respectively, need to be under-recovered in SR16, as discussed in Section 4.1. The predicted Vs from the model of Jackson and Faul (2010) at the base of the crust is 4.75 km/s (Fig. 8C), which is higher than the maximum velocity in either SR16 for this location or in the “Modified Continental” cluster (4.6 km/s). Constraints on uppermost mantle P wave velocities for this region, derived from Pn travel times measured at Transportable Array stations, yield velocities near 8.2 km/s (Buehler and Shearer, 2017). These would imply Vs values of 4.7 to 4.8 km/s for Vp/Vs ratios of 1.7 to 1.8, respectively, and so tentatively support our preferred model. In any case, the CAA can only be present beneath the mountains and may not extend to the coast. This is again consistent with constraints from MT and Sp receiver function observations (Evans et al., 2019).

The CAA, with anomalous values of both Vs and Qp, lies beneath the locus of the youngest known volcanism on the Eastern North American passive margin (∼48 Ma) (Mazza et al., 2016, 2014). The potential temperature of the primary melts was low enough that a mantle plume is not required; instead, delamination of the mantle lithosphere is sufficient to explain volcanism at the passive margin (Mazza et al., 2014, 2016). Our inference of a narrow region of thinned lithosphere beneath the region of volcanic activity is consistent with this hypothesis. The particular mechanism of delamination for lithospheric loss is not strictly required, but successfully explains both the seismic and petrologic observations. Because the topography of the central Appalachian Mountains is compensated by a dense crustal root (Fischer, 2002; Long et al., 2019), we do not infer mantle support of the high topography of the modern Appalachians.

The volume of missing lithosphere is minor in a global context. Approximating the body of delaminated lithosphere as a cylinder with a radius of 50 km extending from 60 km (the shallowest depth of melting in Mazza et al., 2016, 2014) to a depth of 100 or 200 km, we estimate its volume to be 3.1×10^5 to 1.1×10^6 km^3, respectively. For context, subducting a 50 km thick slab to 200 km depth (approximately the depth to which the Juan de Fuca slab appears continuous) along a 1200 km long subduction zone (the approximate length of the modern Cascadia subduction zone) would transport 1.2×10^7 km^3 of lithosphere into the mantle, or one to two orders of magnitude more lithosphere than was lost beneath the Appalachians. Linking the delamination event to the age of the youngest volcanics requires that the mass has left the upper mantle, as the sinking velocity of an instability with a radius of 50 km is on the order of 1 m/yr (Elkins-Tanton, 2007). Today, the lost material has either stalled in the transition zone, sunk towards the core-mantle boundary, or has been assimilated into the background heterogeneity of the mantle.

A likely implication of the asthenosphere being at solidus to super-solidus conditions is that small-scale convection is occurring. Our preferred explanation is “edge-driven” convection because of the steeply dipping LAB. At a step in lithospheric thickness, mantle upwelling will occur behind the “trailing” side of the plate as the asthenosphere must rise to fill the space created by the movement of the lithosphere (e.g., Till et al., 2010). Since the eastern coast of North America represents the “trailing” margin of the continent, a thermal anomaly does not need to be invoked to drive the mantle upwards (e.g., as in King and Anderson, 1998). The physical state of the CAA does require that partial melting be possible, and since the asthenosphere will lie above the solidus for volatile-bearing mantle (Dasgupta et al., 2013; Dasgupta and Hirschmann, 2006) a non-zero melt fraction is expected (Holtzman, 2016).

Small-scale or edge-driven convection has been invoked as an explanation for several seismic anomalies along the margin, particularly beneath New England (Menke et al., 2018, 2016) and in segments beneath South Carolina and Florida (Biryol et al., 2016). Small-scale convection therefore appears to be a common feature beneath the passive margin. However, there seem to be only discrete convection cells along the eastern coast of North America (Biryol et al., 2016; Levin et al., 2018; Lynner and Bodmer, 2017; Menke et al., 2016; Schmandt and Lin, 2014). We speculate that upwellings occur in places of lithospheric removal, and not along the entire passive margin as low *Vs* anomalies appear as localized features rather than a continuous sheet parallel to the coast (Biryol et al., 2016; Schmandt and Lin, 2014).

5. Conclusions

Measurements of seismic attenuation along the MAGIC array from northwest Ohio to the Virginian coast reveal striking and abrupt topography on the base of the North American lithosphere. We identify three distinct domains that correspond to Proterozoic lithosphere, the crest of the Appalachian Mountains, and the Phanerozoic terranes on the eastern coast. We infer loss of the mantle lithosphere from a 100 km wide region beneath the crest of the central Appalachian Mountains, resulting in a strongly attenuating upper mantle. Estimated values of Qp from this study, together with *Vs* constraints from previously published tomography models, suggest that melting processes during upwelling are the likely cause of the “Central Appalachian Anomaly”. The proximity of the partially molten asthenosphere to a steep lithosphere-asthenosphere boundary and young volcanism suggests that edge-driven convection occurs where the lithosphere has been removed by delamination.

Acknowledgements

Funding for this study was provided by the University of Minnesota and by the National Science Foundation (NSF) under grant EAR-1827277 to the University of Minnesota, EAR-1251515 to Yale University, and EAR-1460257 to the College of New Jersey. Data from the MAGIC experiment (network code 7A) were used in this study and can be downloaded from the Incorporated Research Institutions for Seismology (IRIS) Data Management Center (DMC) at http://ds.iris.edu. Seismic instruments were provided by the IRIS PASSCAL Instrument Center at New Mexico Tech. The facilities of the IRIS Consortium are supported by NSF under Cooperative Agreement EAR-1261681 and the DOE National Nuclear Security Administration. The NSF I/D program helped support preparation of this manuscript. Any opinion, findings, and conclusions or recommendations expressed in this article are those of the authors and do not necessarily reflect the views of the National Science Foundation. Fig. 1 was prepared with the GMT/MATLAB toolbox (Wessel and Luis, 2017). We thank two anonymous reviewers and Benjamin Murphy for providing thoughtful and constructive feedback on this manuscript. We extend our thanks to Zachary C. Eilon for making the code of Eilon et al. (2018) publicly available, as reference to this code was necessary to construct the inversion of this study.

Appendix A. Supplementary material

Supplementary material related to this article can be found online at https://doi.org/10.1016/j.epsl.2019.04.045.

References

Abers, G.A., Fischer, K.M., Hirth, G., Wiens, D.A., Plank, T., Holtzman, B.K., McCarthy, C., Gazel, E., 2014. Reconciling mantle attenuation-temperature relationships from seismology, petrology, and laboratory measurements. Geochem. Geophys. Geosyst. 15, 3521–3542. https://doi.org/10.1002/2014GC005444.

Abt, D.L., Fischer, K.M., French, S.W., Ford, H.A., Yuan, H., Romanowicz, B., 2010. North American lithospheric discontinuity structure imaged by Ps and Sp receiver functions. J. Geophys. Res. 115, B09301. https://doi.org/10.1029/2009JB006914.

Adams, D.C., Humphreys, E.D., 2010. New constraints on the properties of the Yellowstone mantle plume from P and S wave attenuation tomography. J. Geophys. Res. 115, B12311. https://doi.org/10.1029/2009JB006864.

Allen, R.M., Nolet, G., Morgan, W.J., Vogfjörd, K., Bergsson, B.H., Erlendsson, P., Foulger, G.R., Jakobsdóttir, S., Julian, B.R., Pritchard, M., Ragnarsson, S., Stefánsson, R., 1999. The thin hot plume beneath Iceland. Geophys. J. Int. 137, 51–63. https://doi.org/10.1046/j.1365-246x.1999.00753.x.

Aragon, J.C., Long, M.D., Benoit, M.H., 2017. Lateral variations in SKS splitting across the MAGIC array, Central Appalachians. Geochem. Geophys. Geosyst. 18, 4136–4155. https://doi.org/10.1002/2017GC007169.

Bao, X., Dalton, C.A., Jin, G., Gaherty, J.B., Shen, Y., 2016. Imaging Rayleigh wave attenuation with USArray. Geophys. J. Int. 206, 241–259. https://doi.org/10.1093/gji/ggw151.

Bezada, M.J., 2017. Insights into the lithospheric architecture of Iberia and Morocco from teleseismic body-wave attenuation. Earth Planet. Sci. Lett. 478, 14–26. https://doi.org/10.1016/j.epsl.2017.08.029.

Bezada, M.J., Byrnes, J.S., Eilon, Z.C., 2019. On the robustness of attenuation measurements on teleseismic P waves: insights from micro-array analysis of the 2017 North Korean nuclear test. Geophys. J. Int. 218, 573–585. https://doi.org/10.1093/gji/ggz169.

Biryol, C.B., Wagner, L.S., Fischer, K.M., Hawman, R.B., 2016. Relationship between observed upper mantle structures and recent tectonic activity across the Southeastern United States. J. Geophys. Res., Solid Earth 121, 3393–3414. https://doi.org/10.1002/2015JB012698.

Bodin, T., Sambridge, M., Rawlinson, N., Arroucau, P., 2012a. Transdimensional tomography with unknown data noise. Geophys. J. Int. 189, 1536–1556. https://doi.org/10.1111/j.1365-246X.2012.05414.x.

Bodin, T., Sambridge, M., Tkalčić, H., Arroucau, P., Gallagher, K., Rawlinson, N., 2012b. Transdimensional inversion of receiver functions and surface wave dispersion. J. Geophys. Res., Solid Earth 117. https://doi.org/10.1029/2011JB008560.

Buehler, J.S., Shearer, P.M., 2017. Uppermost mantle seismic velocity structure beneath USArray. J. Geophys. Res., Solid Earth 122, 436–448. https://doi.org/10.1002/2016JB013265.

Cafferky, S., Schmandt, B., 2015. Teleseismic P wave spectra from USArray and implications for upper mantle attenuation and scattering. Geochem. Geophys. Geosyst. 16, 3343–3361. https://doi.org/10.1002/2015GC005993.

Campbell, K.W., 2009. Estimates of shear-wave Q and κ_0 for unconsolidated and semiconsolidated sediments in Eastern North America estimates of shear-wave Q and κ_0 for sediments in North America. Bull. Seismol. Soc. Am. 99, 2365–2392. https://doi.org/10.1785/0120080116.

Dalton, C.A., Ekström, G., 2006. Global models of surface wave attenuation. J. Geophys. Res. 111, B05317. https://doi.org/10.1029/2005JB003997.

Dasgupta, R., Hirschmann, M.M., 2006. Melting in the Earth's deep upper mantle caused by carbon dioxide. Nature 440, 659. https://doi.org/10.1038/nature04612.

Dasgupta, R., Mallik, A., Tsuno, K., Withers, A.C., Hirth, G., Hirschmann, M.M., 2013. Carbon-dioxide-rich silicate melt in the Earth's upper mantle. Nature 493, 211–215. https://doi.org/10.1038/nature11731.

Eilon, Z., Fischer, K.M., Dalton, C.A., 2018. An adaptive Bayesian inversion for upper-mantle structure using surface waves and scattered body waves. Geophys. J. Int. 214, 232–253. https://doi.org/10.1093/gji/ggy137.

Elkins-Tanton, L.T., 2007. Continental magmatism, volatile recycling, and a heterogeneous mantle caused by lithospheric gravitational instabilities. J. Geophys. Res., Solid Earth 112. https://doi.org/10.1029/2005JB004072.

Evans, R.L., Benoit, M.H., Long, M.D., Elsenbeck, J., Ford, H.A., Zhu, J., Garcia, X., 2019. Thin lithosphere beneath the central Appalachian Mountains: a combined seismic and magnetotelluric study. Earth Planet. Sci. Lett. 519, 308–316. https://doi.org/10.1016/j.epsl.2019.04.046.

Fischer, K.M., 2002. Waning buoyancy in the crustal roots of old mountains. Nature 417, 933–936. https://doi.org/10.1038/nature00855.

Gilligan, A., Bastow, I.D., Watson, E., Darbyshire, F.A., Levin, V., Menke, W., Lane, V., Hawthorn, D., Boyce, A., Liddell, M.V., Petrescu, L., 2016. Lithospheric deformation in the Canadian Appalachians: evidence from shear wave splitting. Geophys. J. Int. 206, 1273–1280. https://doi.org/10.1093/gji/ggw207.

Gribenko, A.V., Zhdanov, M.S., 2017. 3-D inversion of the MT Earth scope data, collected over the East Central United States. Geophys. Res. Lett. 44, 11,800–11,807. https://doi.org/10.1002/2017GL075000.

Hammond, W.C., Humphreys, E.D., 2000. Upper mantle seismic wave attenuation: effects of realistic partial melt distribution. J. Geophys. Res. 105, 10987–10999. https://doi.org/10.1029/2000JB900042.

Hatcher, R.D., 2007. Tectonic map of the southern and central Appalachians: a tale of three orogens and a complete Wilson cycle. In: Hatcher, R.D. (Ed.), 4-D Framework of Continental Crust. Geological Society of America.

Hatcher, R.D., 2010. The Appalachian orogen: a brief summary. In: Geological Society of America Memoirs. Geological Society of America, pp. 1–19.

Herzberg, C., Asimow, P.D., Arndt, N., Niu, Y., Lesher, C.M., Fitton, J.G., Cheadle, M.J., Saunders, A.D., 2007. Temperatures in ambient mantle and plumes: constraints from basalts, picrites, and komatiites. Geochem. Geophys. Geosyst. 8. https://doi.org/10.1029/2006GC001390.

Holtzman, B.K., 2016. Questions on the existence, persistence, and mechanical effects of a very small melt fraction in the asthenosphere. Geochem. Geophys. Geosyst. 17, 470–484. https://doi.org/10.1002/2015GC006102.

Hopper, E., Fischer, K.M., Wagner, L.S., Hawman, R.B., 2017. Reconstructing the end of the Appalachian orogeny. Geology 45, 15–18. https://doi.org/10.1130/G38453.1.

Hwang, Y.K., Ritsema, J., Goes, S., 2009. Spatial variations of P wave attenuation in the mantle beneath North America. J. Geophys. Res. 114, B06312. https://doi.org/10.1029/2008JB006091.

Jackson, I., Faul, U.H., 2010. Grainsize-sensitive viscoelastic relaxation in olivine: towards a robust laboratory-based model for seismological application. In: Special Issue on Deep Slab and Mantle Dynamics. Phys. Earth Planet. Inter. 183, 151–163. https://doi.org/10.1016/j.pepi.2010.09.005.

Karato, S., Spetzler, H.A., 1990. Defect microdynamics in minerals and solid-state mechanisms of seismic wave attenuation and velocity dispersion in the mantle. Rev. Geophys. 28, 399–421. https://doi.org/10.1029/RG028i004p00399.

King, S.D., Anderson, D.L., 1998. Edge-driven convection. Earth Planet. Sci. Lett. 160, 289–296. https://doi.org/10.1016/S0012-821X(98)00089-2.

Knight, K.B., Nomade, S., Renne, P.R., Marzoli, A., Bertrand, H., Youbi, N., 2004. The Central Atlantic Magmatic Province at the Triassic–Jurassic boundary: paleomagnetic and ^{40}Ar/^{39}Ar evidence from Morocco for brief, episodic volcanism. Earth Planet. Sci. Lett. 228, 143–160. https://doi.org/10.1016/j.epsl.2004.09.022.

Lekić, V., Romanowicz, B., 2011a. Tectonic regionalization without a priori information: a cluster analysis of upper mantle tomography. Earth Planet. Sci. Lett. 308, 151–160. https://doi.org/10.1016/j.epsl.2011.05.050.

Lekić, V., Romanowicz, B., 2011b. Inferring upper-mantle structure by full waveform tomography with the spectral element method. Geophys. J. Int. 185, 799–831. https://doi.org/10.1111/j.1365-246X.2011.04969.x.

Levin, V., Long, M.D., Skryzalin, P., Li, Y., López, I., 2018. Seismic evidence for a recently formed mantle upwelling beneath New England. Geology 46, 87–90. https://doi.org/10.1130/G39641.1.

Li, Y., 2013. Post 23 August 2011 Mineral, Virginia, earthquake investigations at North Anna nuclear power plant. Seismol. Res. Lett. 84, 468–473. https://doi.org/10.1785/0220120179.

Long, M.D., Jackson, K.G., McNamara, J.F., 2016. SKS splitting beneath Transportable Array stations in eastern North America and the signature of past lithospheric deformation. Geochem. Geophys. Geosyst. 17, 2–15. https://doi.org/10.1002/2015GC006088.

Long, M.D., Benoit, M.H., Aragon, J.C., King, S.D., 2019. Seismic imaging of mid-crustal structure beneath central and eastern North America: possibly the elusive Grenville deformation? Geology 47, 371–374. https://doi.org/10.1130/G46077.1.

Lynner, C., Bodmer, M., 2017. Mantle flow along the eastern North American margin inferred from shear wave splitting. Geology 45, 867–870. https://doi.org/10.1130/G38980.1.

Malinverno, A., Briggs, V.A., 2004. Expanded uncertainty quantification in inverse problems: hierarchical Bayes and empirical Bayes. Geophysics 69, 1005–1016. https://doi.org/10.1190/1.1778243.

Marzoli, A., Renne, P.R., Piccirillo, E.M., Ernesto, M., Bellieni, G., Min, A.D., 1999. Extensive 200-million-year-old continental flood basalts of the Central Atlantic Magmatic Province. Science 284, 616–618. https://doi.org/10.1126/science.284.5414.616.

Marzoli, A., Bertrand, H., Knight, K.B., Cirilli, S., Buratti, N., Vérati, C., Nomade, S., Renne, P.R., Youbi, N., Martini, R., Allenbach, K., Neuwerth, R., Rapaille, C., Zaninetti, L., Bellieni, G., 2004. Synchrony of the Central Atlantic magmatic province and the Triassic-Jurassic boundary climatic and biotic crisis. Geology 32, 973. https://doi.org/10.1130/G20652.1.

Mazza, S.E., Gazel, E., Johnson, E.A., Kunk, M.J., McAleer, R., Spotila, J.A., Bizimis, M., Coleman, D.S., 2014. Volcanoes of the passive margin: the youngest magmatic event in eastern North America. Geology 42, 483–486. https://doi.org/10.1130/G35407.1.

Mazza, S.E., Gazel, E., Johnson, E.A., Bizimis, M., McAleer, R., Biryol, C.B., 2016. Post-rift magmatic evolution of the eastern North American "passive-aggressive" margin. Geochem. Geophys. Geosyst. 18, 3–22. https://doi.org/10.1002/2016GC006646.

Menke, W., Skryzalin, P., Levin, V., Harper, T., Darbyshire, F., Dong, T., 2016. The Northern Appalachian Anomaly: a modern asthenospheric upwelling. Geophys. Res. Lett. 43, 10,173–10,179. https://doi.org/10.1002/2016GL070918.

Menke, W., Lamoureux, J., Abbott, D., Hopper, E., Hutson, D., Marrero, A., 2018. Crustal heating and lithospheric alteration and erosion associated with asthenospheric upwelling beneath Southern New England (USA). J. Geophys. Res., Solid Earth 123, 8995–9008. https://doi.org/10.1029/2018JB015921.

Miller, S.R., Sak, P.B., Kirby, E., Bierman, P.R., 2013. Neogene rejuvenation of central Appalachian topography: evidence for differential rock uplift from stream profiles and erosion rates. Earth Planet. Sci. Lett. 369–370, 1–12. https://doi.org/10.1016/j.epsl.2013.04.007.

Müller, R.D., Seton, M., Zahirovic, S., Williams, S.E., Matthews, K.J., Wright, N.M., Shephard, G.E., Maloney, K.T., Barnett-Moore, N., Hosseinpour, M., Bower, D.J., Cannon, J., 2016. Ocean basin evolution and global-scale plate reorganization events since Pangea breakup. Annu. Rev. Earth Planet. Sci. 44, 107–138. https://doi.org/10.1146/annurev-earth-060115-012211.

Murphy, B.S., Egbert, G.D., 2017. Electrical conductivity structure of southeastern North America: implications for lithospheric architecture and Appalachian topographic rejuvenation. Earth Planet. Sci. Lett. 462, 66–75. https://doi.org/10.1016/j.epsl.2017.01.009.

Olugboji, T.M., Lekic, V., McDonough, W., 2017. A statistical assessment of seismic models of the U.S. continental crust using Bayesian inversion of ambient noise surface wave dispersion data. Tectonics 36, 1232–1253. https://doi.org/10.1002/2017TC004468.

Richards, P.G., Menke, W., 1983. The apparent attenuation of a scattering medium. Bull. Seismol. Soc. Am. 73, 1005–1021.

Rowley, D.B., Forte, A.M., Moucha, R., Mitrovica, J.X., Simmons, N.A., Grand, S.P., 2013. Dynamic topography change of the Eastern United States since 3 million years ago. Science 340, 1560–1563. https://doi.org/10.1126/science.1229180.

Rychert, C.A., Fischer, K.M., Rondenay, S., 2005. A sharp lithosphere–asthenosphere boundary imaged beneath eastern North America. Nature 436, 542–545. https://doi.org/10.1038/nature03904.

Rychert, C.A., Rondenay, S., Fischer, K.M., 2007. P-to-S and S-to-P imaging of a sharp lithosphere-asthenosphere boundary beneath eastern North America. J. Geophys. Res., Solid Earth 112. https://doi.org/10.1029/2006JB004619.

Sarafian, E., Gaetani, G.A., Hauri, E.H., Sarafian, A.R., 2017. Experimental constraints on the damp peridotite solidus and oceanic mantle potential temperature. Science 355, 942–945. https://doi.org/10.1126/science.aaj2165.

Savage, B., Covellone, B.M., Shen, Y., 2017. Wave speed structure of the eastern North American margin. Earth Planet. Sci. Lett. 459, 394–405. https://doi.org/10.1016/j.epsl.2016.11.028.

Schaeffer, A.J., Lebedev, S., 2014. Imaging the North American continent using waveform inversion of global and USArray data. Earth Planet. Sci. Lett. 402, 26–41. https://doi.org/10.1016/j.epsl.2014.05.014.

Schmandt, B., Lin, F.-C., 2014. P and S wave tomography of the mantle beneath the United States. Geophys. Res. Lett. 41, 2014GL061231. https://doi.org/10.1002/2014GL061231.

Shen, W., Ritzwoller, M.H., 2016. Crustal and uppermost mantle structure beneath the United States. J. Geophys. Res., Solid Earth 121, 2016JB012887. https://doi.org/10.1002/2016JB012887.

Southworth, C.S., Gray, K., Sutter, J.F., 1993. Middle Eocene intrusive igneous rocks of the central Appalachian Valley and Ridge Province: setting, chemistry and implications for crustal structure. U.S. Geol. Surv. Bull. B1839-J, J1–J24.

Takei, Y., 2017. Effects of partial melting on seismic velocity and attenuation: a new insight from experiments. Annu. Rev. Earth Planet. Sci. 45, 447–470. https://doi.org/10.1146/annurev-earth-063016-015820.

Teng, T.-L., 1968. Attenuation of body waves and the Q structure of the mantle. J. Geophys. Res. 73, 2195–2208. https://doi.org/10.1029/JB073i006p02195.

Till, C.B., Elkins-Tanton, L.T., Fischer, K.M., 2010. A mechanism for low-extent melts at the lithosphere-asthenosphere boundary. Geochem. Geophys. Geosyst. 11. https://doi.org/10.1029/2010GC003234.

Villagómez, D.R., Toomey, D.R., Hooft, E.E.E., Solomon, S.C., 2007. Upper mantle structure beneath the Galápagos Archipelago from surface wave tomography. J. Geophys. Res., Solid Earth 112. https://doi.org/10.1029/2006JB004672.

Villagómez, D.R., Toomey, D.R., Geist, D.J., Hooft, E.E.E., Solomon, S.C., 2014. Mantle flow and multistage melting beneath the Galapagos hotspot revealed by seismic imaging. Nat. Geosci. 7, 151–156. https://doi.org/10.1038/ngeo2062.

Wessel, P., Luis, J.F., 2017. The GMT/MATLAB toolbox. Geochem. Geophys. Geosyst. 18, 811–823. https://doi.org/10.1002/2016GC006723.

Whitmeyer, S.J., Karlstrom, K.E., 2007. Tectonic model for the Proterozoic growth of North America. Geosphere 3, 220–259. https://doi.org/10.1130/GES00055.1.

Wu, R.-S., 1982. Attenuation of short period seismic waves due to scattering. Geophys. Res. Lett. 9, 9–12. https://doi.org/10.1029/GL009i001p00009.

Yamauchi, H., Takei, Y., 2016. Polycrystal anelasticity at near-solidus temperatures. J. Geophys. Res., Solid Earth 121, 2016JB013316. https://doi.org/10.1002/2016JB013316.

Yang, X., Gao, H., 2018. Full-wave seismic tomography in the Northeastern United States: new insights into the uplift mechanism of the Adirondack Mountains. Geophys. Res. Lett. 45, 5992–6000. https://doi.org/10.1029/2018GL078438.

Yuan, H., French, S., Cupillard, P., Romanowicz, B., 2014. Lithospheric expression of geological units in central and eastern North America from full waveform tomography. Earth Planet. Sci. Lett. 402, 176–186. https://doi.org/10.1016/j.epsl.2013.11.057.